Maximizing Transfection Efficiency of Vertically Aligned Silicon Nanowire Arrays

*Roey Elnathan, Bahman Delalat, Daniel Brodoceanu, Hashim Alhmoud, Frances J. Harding, Katrin Buehler, Adrienne Nelson, Lucio Isa, Tobias Kraus, and Nicolas H. Voelcker**

Vertically aligned silicon nanowire (VA-SiNW) arrays are emerging as a powerful new tool for gene delivery by means of mechanical transfection. In order to utilize this tool efficiently, uncertainties around the required design parameters need to be removed. Here, a combination of nanosphere lithography and templated metal-assisted wet chemical etching is used to fabricate VA-SiNW arrays with a range of diameters, heights, and densities. This fabrication strategy allows identification of critical parameters of surface topography and consequently the design of SiNW arrays that deliver plasmid with high transfection efficiency into a diverse range of human cells whilst maintaining high cell viability. These results illuminate the cell-materials interactions that mediate VA-SiNW transfection and have the potential to transform gene therapy and underpin future treatment modalities.

1. Introduction

Gene therapy is now a viable strategy for treating a number of disorders.[1] Clinical proof-of-concept treatments have been demonstrated for diseases including hemophilia B, retinal disease, and chronic lymphocytic leukemia.[2–4] New genetic material, such as DNA or siRNA, is introduced into targeted cells to induce a therapeutic response for patient benefit.[5] One of the current impediments to successful gene therapy is the inefficient delivery of the corrective nucleic acid code into target cells. New methods are required to deliver nucleic acid reagents into diverse cell types effectively and with high yields. Promising results have been obtained using 1D nanomaterials, such as silicon nanowires (SiNW),[6] nanostraws,[7] hollow nanoneedles,[8] carbon nanotubes,[9] and nanofibers[10] to transfect mammalian cells.

Vertically aligned silicon nanowire (VA-SiNW) arrays are an emerging platform applicable across several life science contexts, including biosensors and cell scaffolds.[11,12] Various reports have demonstrated that NW arrays can achieve intimate and nontoxic interactions with mammalian cells.[7,13,14] SiNW arrays can be employed as physical nanotopographical cues to elicit specific cell responses and as vectors for delivering biomolecular cargo into a wide range of mammalian cells.[6,15] NW-mediated transfection is not only compatible with continued cell viability, adhesion, and proliferation, it bypasses the limitations inherent to endocytotic uptake mechanisms and directly transports exogenous materials into the cell interior.[16–19] NW-mediated transfection is a form of mechanical transfection that is attributed to an "impaling mechanism," in which penetration by vertically aligned NW is driven predominantly by cell adhesion to the substrate and initiated soon after the application of cells to the NW array.[20,21] Attempts to enhance the intracellular access process have been carried out by applying force to the NW–cell interface,[22] by coating the NW with aminosilane and other cell adhesion promoting molecules,[21,23] or by electroporation,[24] as well as by adding membrane destabilizer molecules such as saponin to increase the odds of membrane penetration.[8]

Han et al.[25] were the first to demonstrate the insertion of DNA into living cells using a DNA-functionalized atomic force microscopy (AFM) tip. In a follow-up study, the authors inserted plasmid DNA (pDNA) into the nucleus of primary human mesenchymal stem cells (hMSCs) and reported 74% GFP expression efficiency.[25,26] By using vertically aligned arrays of SiNW to deliver plasmid DNA, Kim and colleagues were able to expand this from a cell by cell procedure to a platform able to transfect of many cells in parallel.[13] Despite the poor transfection efficiency reported, this pivotal work provided experimental evidence for the feasibility of directly accessing the cell interior using NW. In 2010, a fundamental advance in the field emerged from the Park laboratory. They used SiNW prepared by vapor–liquid–solid (VLS) chemical vapor deposition (CVD) to deliver a broad range of fluorescently labeled biomolecules

Dr. R. Elnathan, Dr. B. Delalat, H. Alhmoud, Dr. F. J. Harding, K. Buehler, Prof. N. H. Voelcker
ARC Centre of Excellence in Convergent Bio-Nano Science and Technology
Mawson Institute
University of South Australia
Mawson Lakes 5095, Australia
E-mail: nico.voelcker@unisa.edu.au
Dr. D. Brodoceanu, Dr. T. Kraus
INM-Leibniz Institute for New Materials
Campus D2 2, 66123 Saarbrücken, Germany
Dr. A. Nelson, Prof. L. Isa
Laboratory for Interfaces
Soft Matter and Assembly
Department of Materials
ETH Zurich
Vladimir-Prelog-Weg 5, 8093 Zurich, Switzerland

DOI: 10.1002/adfm.201503465

(such as DNA plasmids, siRNAs, peptides, proteins, and other small molecules) into a number of cell types, including primary cells, with a reported efficiency as high as ≈95%.[6] In a second study, Shalek et al. prepared VA-SiNW arrays by VLS-CVD for gene silencing in immune cell subsets that are considered particularly difficult to transfect.[27] The dimensions and spacing of the vertical SiNW arrays were optimized for each cell type. Recently, mesoporous VA-SiNW arrays have been demonstrated to directly transport quantum dots loaded into the pore structure across the cell membrane and into the cytosol.[28] Similar degradable arrays have been translated into vectors for localized gene therapy in vivo, able to inject plasmid DNA into skin and muscle tissue.[29]

Given the staggering complexity of cellular processes, even subtle variations in the physical geometrical parameters of NW arrays (density,[30] diameter,[12] and height[31]) may elicit dramatic changes to cell morphology,[32] adhesion,[33] maturation, and penetration by NW elements.[11,12,20,34] Thus, randomly positioned NW cannot elicit a reproducible response. Homogeneous and consistent NW platforms with controlled aspect ratio, density, and orientation reduce response variability, aiding the design of topography optimized for gene delivery.

Current NW-based delivery approaches to deliver DNA into mammalian cells employ epitaxial VLS or reactive-ion etching (RIE)-based growth processes to generate arrays of solid NW.[6,13] However, there are drawbacks to these fabrication processes: VLS growth requires specific Si substrates, employs expensive setups to handle hazardous silane gases at high temperatures, and is generally restricted to circular-shaped gold catalysts.[35] Additionally, the limited ability to control positioning, orientation, and density of VLS-generated NW in arrays render studies of NW–cell interactions less useful.[12] RIE limits NW aspect ratio and remains a costly and cumbersome method.

In contrast, a combination of nanosphere lithography (NSL) and templated metal-assisted wet chemical etching (tMACE) offers a promising alternative solution to high-cost conventional lithographical patterning and epitaxial VLS- and RIE-based growth processes,[36] enabling precise positioning of the individual SiNW elements with controlled diameter, length, and density.[37] An inherent limitation of this combined approach is the coupling of NW diameter and spacing by the size of the polystyrene nanospheres (PSNS) used as a shadow mask. The two parameters cannot be changed independently on the same substrate. Decoupling of NW spacing and diameter can be achieved to an extent by plasma treatment to reduce the size of PSNS, but eventually the morphology of the etched PSNS deviates from spherical. As such, we also employed a different fabrication route, namely particle self-assembly at liquid–liquid interfaces (SALI), which engenders greater control over the etching sites on the surface surface.[38] Studies in the field have exploited top-down and bottom-up approaches to fabricate patterned and randomly distributed arrays of vertically aligned semiconductor NW arrays to investigate cell function and behavior.[17,30,31,39–42] However, no one has exploited the combination of NSL and tMACE as an affordable approach to fabricate patterned VA-SiNW arrays for gene delivery applications.

Here, we examine the effect of geometrical parameters of ordered SiNW arrays formed by tMACE on transfection efficiency in human cells. By combining NSL techniques such as convective assembly and SALI with tMACE processes, we can tune SiNW array geometries to achieve highly efficient cell transfection in a range of human cell types. We suggest that the use of this simple, low-cost, and versatile fabrication approach enables true control of the relevant fabrication parameters and will benefit the gene delivery field significantly and increase the use of this exciting technology.

2. Results and Discussion

2.1. Assembly of Ordered, Uniform PSNS Arrays

A combination of NSL based on the self-assembly of PSNS and tMACE was used to fabricate ordered SiNW arrays. This process involved several distinct steps, summarized in **Scheme 1**. Fabrication starts with self-assembly of a hexagonal close-packed (hcp) 2D array of PSNS over a large area of a Si wafer. At the outset, we used spin coating to rapidly deposit PSNS in an hcp array on the Si surface. However, this approach was not suitable for the construction of large-scale, dense, and uniform hcp monolayer arrays since a large number of voids with stochastic arrangement were produced (Figure S1a, Supporting Information). Upon performing tMACE, the stochastic arrangement translated into a random pattern of SiNW arrays (Figure S1b, Supporting Information). To circumvent this problem, a different deposition technique, convective assembly, was used to create uniform, large-scale, and dense hcp monolayers of PSNS on Si substrates (Scheme 1a). The assembly mechanism is based on the convective flow of a solvent, induced by evaporation at the contact line of a droplet of PSNS suspension; on flat surfaces this leads to the formation of continuous 2D films of packed PSNS (Scheme 1b). By adjusting four key experimental parameters in the convective assembly method—PSNS size, concentration, deposition speed, and Si hydrophilicity—we were able to fabricate well-ordered monolayer of PSNS with diameters ranging from 300 to 1000 nm with wafer-scale uniformity within minutes. This approach not only allowed us to control the size of self-assembled PSNS conveniently but also to eliminate the formation of large random voids in the PSNS monolayer.

The resulting hcp monolayer arrays were converted into non-close-packed (ncp) monolayer arrays using O_2 plasma etching (Scheme 1c). By careful modulation of the plasma process parameters (etching duration, power, and other conditions), we were able to produce final PSNS diameters down to 150 nm in diameter (Figure S2f, Supporting Information). The size and precise location of the etched PSNS dictates the geometry and morphology of the individual NW elements within the array.[43]

The next step in the fabrication of SiNW arrays was the formation of the continuous Ag catalyst layer on top of the PSNS arrays (Scheme 1d and Figure S2b, Supporting Information). The thickness of the catalyst Ag layer ranged between 20 and 40 nm, depending on the diameter of the PSNS. The PSNS were then selectively removed through a lift-off process (Scheme 1e and Figure S2c, Supporting Information), leaving behind only the Ag deposited through the mask. A complementary colloidal self-assembly strategy, self-assembly SALI, was employed to produce a low-density array of PSNS on the Si surface. Using

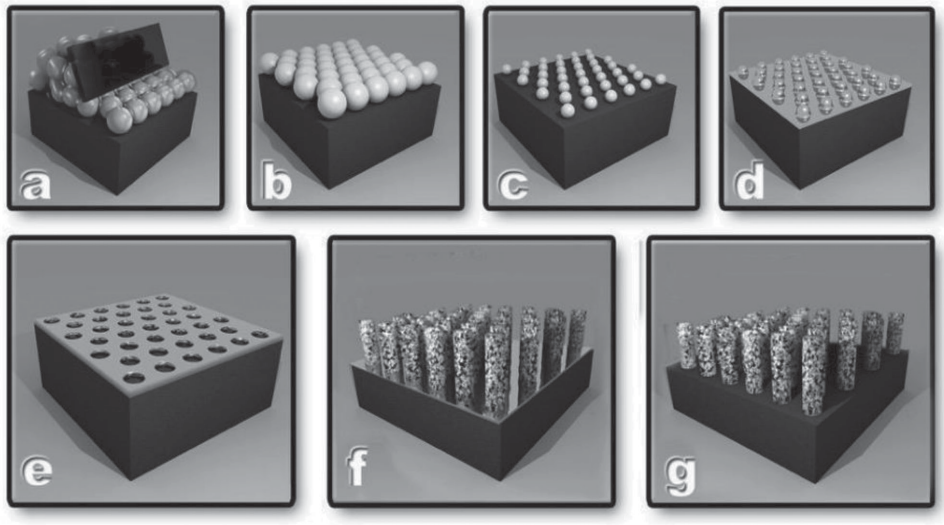

Scheme 1. Fabrication of VA-SiNW arrays using tMACE. a) PSNS were convectively assembled on a Si wafer. b) A hexagonal close-packed (hcp) monolayer of monodisperse PSNS was assembled via convective assembly and then c) transferred into a nonclose-packed (ncp) PSNS array via O_2 plasma etching. d) The array was used as a mask for Ag metal layer deposition by sputter coating. e) After removing the PSNS by lift off, an ordered array of holes was produced in the Ag film. Subsequently, the metal layer served as a catalyst for the wet etching of silicon by MACE. f) Using this method, arrays of vertically aligned SiNW arrays were fabricated with different aspect ratios. g) The Ag layer was finally removed with nitric acid.

this technique, the PSNS density could be modulated through process parameters such as PSNS concentration, choice of solvent, and the speed of Si substrate extraction through the SALI interface (details in the experimental section).

2.2. Fabrication of SiNW Arrays

The perforated Ag layer deposited on the Si was used as a catalyst material for the synthesis of VA-SiNW arrays by tMACE, followed by the removal of the Ag layer by nitric acid (Scheme 1f,g). The process yielded SiNW arrays that replicated the lateral geometry of the PSNS monolayer shadow mask with high fidelity. Ordered VA-SiNW array architectures were fabricated by means of the tMACE process (**Figure 1**).

The inset in Figure 1 reveals the nanoscale roughness of the SiNW. Using AFM, we observed that fabricated SiNW exhibited a small degree of porosity with an average peak-to-valley roughness of 3.8 nm (Figure S3a, Supporting Information). This is in contrast to SiNW arrays fabricated via epitaxial VLS- and RIE-based growth techniques, which result in smooth and solid SiNW. Structural characterization by high-resolution transmission electron microscopy (HR-TEM) images confirmed the porous nature of SiNW (Figure S3b–d, Supporting Information). Porosity increases from the base to the tip of the wire (Figure S4, Supporting Information). Porous SiNW possess several advantages for drug and gene delivery applications.[29] The incorporation of porosity to the NW structure increases the surface area available for loading of therapeutic molecules.

Further, these porous SiNW degraded under cell culture conditions and at the point of contact with the cells, resulting in significant decreases in NW diameter (Figure S5, Supporting Information). This is a well-known phenomenon for porous silicon and has been observed for other porous SiNW.[34,44,45] It is possible that the porous nature of these SiNW will in itself enhances cell adhesion.[16,46,47]

2.3. Cell Transfection Using SiNW Arrays

We used the ordered SiNW arrays generated to assess how array geometry affects the efficacy of cell transfection across four human cell types: two human immortalized cell lines (HEK293 and HeLa) and two human primary cell types (human dental pulp stem cells, hDPSC and human foreskin fibroblasts, HFF). A range of SiNW array architectures (NW average dimensions of 330–600 nm diameter, 0.4–6.3 μm height, and 0.6–4.0 SiNW μm^{-2} density) were used for this investigation. gWizTM high-expression enhanced green fluorescent protein vector (gWizTM eGFP) was employed as a reporter gene for successful plasmid DNA transfection. The SiNW arrays were first coated with poly-D-lysine (PDL) in order to allow plasmid sorption via electrostatic interactions and promote cell adhesion.[48]

We first examined the combined influence of SiNW diameter and height on the delivery of eGFP plasmid into primary hDPSC and HEK293 cells. Primary hDPSC, a mesenchymal stem cell population, is responsive to surface topography and has great potential for future cell-based therapeutics.[49] HEK293 cells are often used as model cell line for transfection studies.[13] The majority of previous work into the optimal VA-NW geometry for cell transfection have employed epitaxial VLS-based and RIE growth processes that are known to generate solid NW with a much narrower range of diameters.[6,14] Here we extend the range of NW diameters to a maximum of 600 nm. The minimum diameter tested, 330 nm, was chosen to confer the SiNW elements with the mechanical strength to withstand the dynamic mechanical forces exerted by the cells, such as adhesion and cytoskeletal reorganization,[50–52]

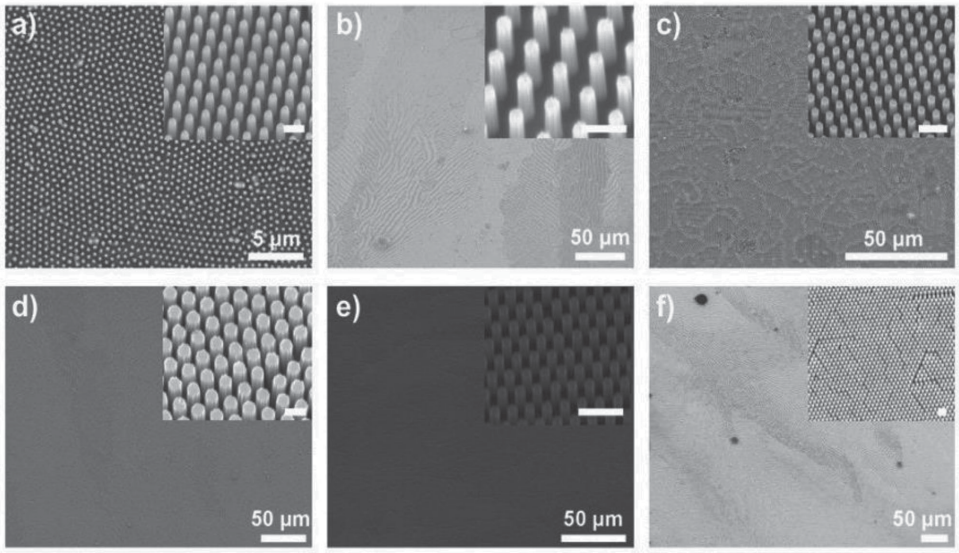

Figure 1. Scanning electron microscopy (SEM) images of VA-SiNW arrays. a–f) Selected top and tilt-view SEM images of SiNW arrays used to systematically investigate the influence of SiNW geometry on the efficacy of cell transfection. Average NW dimensions: a) diameter: 350 nm, length: 1.2 μm, and density: 1 SiNW μm^{-2}; b) diameter: 400 nm, length: 1.2 μm, and density: 1 SiNW μm^{-2}; c) diameter: 250 nm, length: 0.4 μm, and density: 4 SiNW μm^{-2}, d) diameter: 600 nm, length: 3.5 μm, and density: 1 SiNW μm^{-2}, e) diameter: 320 nm, length: 0.4 μm, and density: 4 SiNW μm^{-2}, f) diameter: 300 nm, length: 1.2 μm, and density: 4 SiNW μm^{-2}. Scale bars represent: a) 5 μm and b–f) 50 μm. Insets: corresponding zoom-in SEM images 1 μm.

increasing the likelihood of NW to remain vertical and free-standing during interaction with cells. Similarly, NW average height was limited to a maximum value of 6.3 μm to exclude the undesirable effect of coalescence between the tips of NWs due to Van der Waals forces.[53] Using the approach presented here, SiNW diameter is controlled by particle size. In principle, NW dimensions are unconstrained, and both NW diameter and length could be expanded beyond the range examined here.

Figure 2a,b plots the average transfection efficiency as a function of three SiNW diameters (330, 400, and 600 nm) and

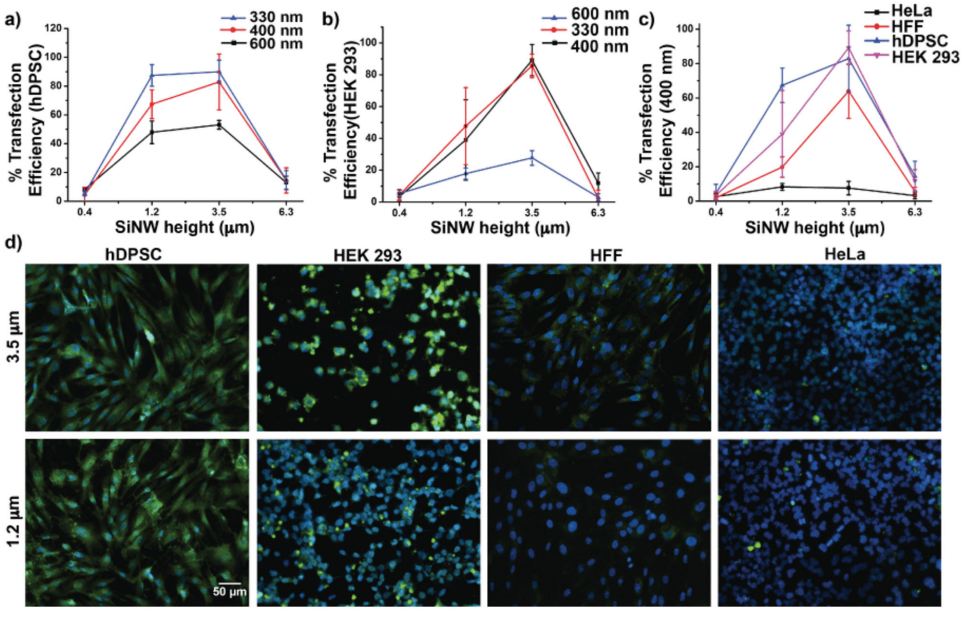

Figure 2. Transfection efficiency is governed by NW geometry and varies according to cell type. a,b) Plot of average eGFP transfection efficiency of primary hDPSC and HEK293 cells, respectively, transfected using SiNW arrays of three different NW diameters (330, 400, and 600 nm) as a function of NW height, at a fixed SiNW density of 1 SiNW μm^{-2}. c) Comparison of average eGFP transfection efficiency results for hDPSC, HEK293, HeLa, and HFF mediated by SiNW arrays (400 nm in diameter) as a function of SiNW height, at a fixed SiNW density of 1 SiNW μm^{-2}. d) Corresponding fluorescence images for transfected hDPSC, HEK293, HFF, and HeLa cells (green color) seeded on SiNW arrays with NW elements of two different NW heights: 1.2 and 3.5 μm, at a fixed SiNW density of 1 SiNW μm^{-2} and a fixed diameter of 400 nm. All cells were costained with nuclear dye Hoechst 33342 (blue color). $N \geq 3$. Error bars describe standard deviation. Scale bar represents 50 μm.

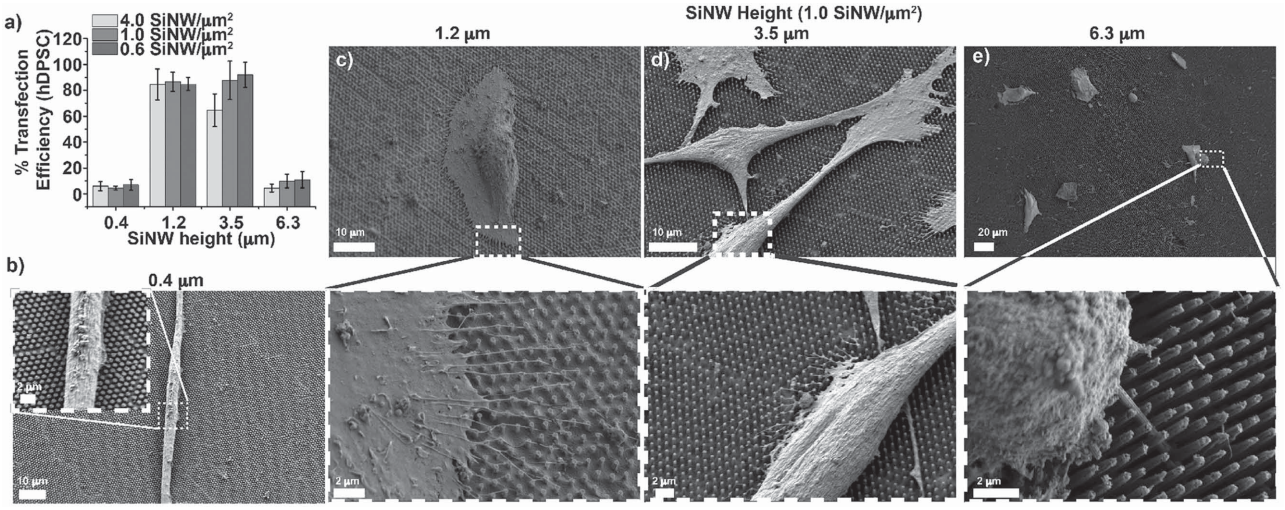

Figure 3. NW height has a greater influence than NW density on transfection efficiency. a) A plot of the average transfection efficiency for primary hDPSC adhering to an array of SiNW of 0.6–4.0 NW μm^{-2} in density (with average diameter of 330 nm as a function of NW height). Arrays of 0.6 NW μm^{-2} density were fabricated via the SALI approach, whereas the fabrication of 1.0 and 4.0 NW μm^{-2} was achieved via the convective assembly. $N \geq 3$. Error bars describe standard deviation. SEM images of hDPSC adhering to SiNW arrays of NW average height: b) 0.4 μm, c) 1.2 μm, d) 3.5 μm, and e) 6.3 μm. Note: Cells in density exhibit marked lamellipodia and filopodia extending to distant NW when cultured on arrays of NW heights 1.2–3.5 μm.

four NW heights (0.4, 1.2, 3.5, and 6.3 μm) for (a) primary hDPSC and (b) HEK293 cells. For this comparison, NW density was fixed at 1 NW μm^{-2}. Notably, for both HEK293 and hDPSC, transfection efficiency was high at NW heights of 1.2 and 3.5 μm, but compromized at the high and low extremes of NW height range examined (0.4 and 6.3 μm). In the case of HEK293 cells, improved transfection efficiency was evident on NWs of height 3.5 μm compared to those of height 1.2 μm ($p < 0.0001$, Fisher's exact test, 2-tailed for all NW diameter series). No significant increase in the rate of hDPSC transfection was observed when NW height was increased from 1.2 to 3.5 μm in the NW diameter range tested. Cell transfection rate was greater on arrays featuring thinner SiNW diameters (330 and 400 nm) for both cell types. However, variation between the maximum transfection efficiencies reported for 330 and 400 nm diameters was negligible. For hDPSC on arrays of 3.5 μm NW height, transfection efficiency was equivalently high for 330 nm diameter ($\eta = 88\%$) and 400 nm diameter ($\eta = 85\%$, $p = 0.35$) NW. Likewise, HEK293 transfection on SiNW of 3.5 μm height was similar on NW of 330 and 400 nm diameter (85% vs 86%, $p = 0.86$).

Fixing NW diameter at 400 nm, the transfection of two additional cell lines, primary fibroblasts (HFF) and HeLa, was examined (Figure 2c). The transfection of HFF cells showed a similar trend in response to NW height to that previously observed for hDPSC and HEK293. Transfection efficiency also peaked on NW arrays of height 3.5 μm. However, the maximum efficiency recorded was lower than that of HEK293 and hDPSC ($\eta = 61\%$, $p < 0.0001$, Fisher's exact test, 2-tailed). A NW diameter of 400 nm and height of 3.5 μm corresponds to an aspect ratio of around 9. This represents an aspect ratio on the lower end of the range employed for VLS-CVD SiNW by Shalek et al.[6,27]

For HeLa cells, low values of transfection efficiencies were observed for all NW heights, indicating that SiNW-based transfection is highly cell type dependent.[12] HeLa transfection efficiency varied little between 1.2 μm ($\eta = 9\%$) and 3.5 μm NW heights ($\eta = 7\%$, $p = 0.3$). Figure 2d shows representative fluorescence microscopy images for transfected hDPSC, HEK293, HFF, and HeLa cells seeded on SiNW arrays with NW elements of 400 nm diameter at two different NW heights, 3.5 and 1.2 μm, at a fixed SiNW density of 1 SiNW μm^{-2}.

SiNW density has been suggested as another determinant of cell transfection efficiency, since the spacing between NWs influences both the morphology and adhesion of cells grown in contact with VA-NW arrays.[30] Next, the interaction between NW density and height was examined using primary hDPSC (**Figure 3**a). Under the conditions examined, the influence of NW density on transfection efficiency was weak when compared to the effect of NW height. This is an intriguing result in light of previous studies emphasizing the importance of NW density on transfection efficiency, implying low pDNA delivery efficiency for NW at high density ("bed-of-nails" effect).[20,54] However, the minimum NW density tested in our study (0.6 NW μm^{-2}) is at least twofold higher than reported previously as optimal for adherent hematopoietic cells using CVD-grown NW (0.15–0.3 NW μm^{-2}),[27] so we cannot rule out a stronger influence of NW density on transfection efficiency at lower ranges than that tested here.

Taken together, our results support a general tendency toward higher transfection efficiency on higher aspect ratio NW arrays as per previous reports.[12,27] However, these results also reveal significant caveats to this generalization. Beyond a critical threshold of NW height at around 3.5 μm, transfection rate was not improved and actually decreased. Whilst similar NW geometry resulted in optimal transfection efficiencies across the four cell types tested, the maximum η value achieved at these optimal conditions varied greatly between cell types. To reinforce the validity of these transfection results, it was critical to explore the NW–cell interactions that govern the phenomena observed: the striking similarity in optimal NW height observed across cell types, contrasting with the variation in the actual transfection efficiency achieved.

2.4. Cell Viability and Proliferation as a Function of SiNW Geometry

For HEK 293, HFF, and hDPSC, maximal η values were observed for SiNW with an average height of 3.5 µm. A further increase in NW height decreased transfection efficiency. Previously, long NW have been associated with decreased cell viability through detrimental interactions with the cell nucleus.[27] Other studies report that increasing NW height impairs cell function and division, and induces DNA damage.[14,55] Thus, we first examined the influence of NW height on cell viability and proliferation (Figures S6 and S7, Supporting Information). VA-SiNW arrays with NW of 400 nm average diameter, 1 SiNW µm^{-2} density, and an average height range of 0.4–6.3 µm were used to evaluate cell viability and proliferation, respectively. Viability was measured directly by staining HEK293, HeLa, HFF, and hDPSC with fluorescein diacetate (FDA) and propidium iodide (PI), whereas cell proliferation was assessed using the Click-iT 5-ethynyl-2′-deoxyuridine (EDU) technique via the labeling of cells containing newly synthesized DNA. Cell viability and proliferation rates were high for SiNW arrays of 3.5 µm NW height across all four cell types examined. Long (6.3 µm height) SiNW caused a sharp decrease in both viability and proliferation. The drop in cell viability and proliferation rate when using long NW would be expected to contribute to the poor transfection efficiencies observed with these NW arrays.

2.5. The Influence of NW Geometry on the Cell-NW Interface

Characterization of the cell-NW interface via SEM, focused ion beam scanning electron microscopy (FIB-SEM), confocal microscopy, and super-resolution structured illumination microscopy (SR-SIM) allowed us to further probe how NW height influences the efficiency of cell transfection. Several modes of cell–NW interaction were evident when observing hDPSC cultured on SiNW elements across the four NW heights examined via SEM (Figure 3b–e). Typically, at the low and high extremes of the NW heights tested (0.4 and 6.3 µm), we observed fewer filopodia extended to interact with the NW topography. In contrast, at intermediate NW heights (1.2–3.5 µm, hDPSC exhibited a highly elongated morphology with distinct lamellipodia and filopodia extending outwards in all directions to the cell body to tether the cell to distant NW (corresponding zoom-in SEM images, Figure 3c,d). For example, for NW arrays of 1.2 µm, cells extended >6 µm long filopodia, and we counted up to 75 filopodia per cell. Moreover, at these two NW heights, NW protrusions on the periphery of the apical cell surface were evident (**Figure 4**a). However, NW did not extend out of the apical cell body surface. The cell membrane was observed to wrap around the NW elements, conforming to the NW shape (Figure 4a(inset),b,c).

Because of this effect, the contact area with the DNA-coated SiNW elements increased, potentially increasing the quantity of DNA presented directly to the cell surface. Additionally, cell membrane curvature induced by interaction with the NW may trigger endocytic pathways that enhance DNA uptake. The accommodation of the NW topography by the cell membrane, combined with the filopodia protrusions contribute to the mechanical strength of the cell–NW interface, enhancing cellular adhesion.[55,56] NW were largely embedded within the membrane without apparent membrane rupture (Figure 4d, red arrow). In confocal microscopy and SR-SIM of transfected hDPSC (Figure 4e,f), individual SiNW elements appear as black dots under the hDPSC, providing further evidence of intimate contact. Elongated hDPSC morphology when cultured on SiNW arrays is evident in the SEM, fluorescence microscopy, and confocal microscopy images (Figures 2d, 3d, and 4a,e,f).

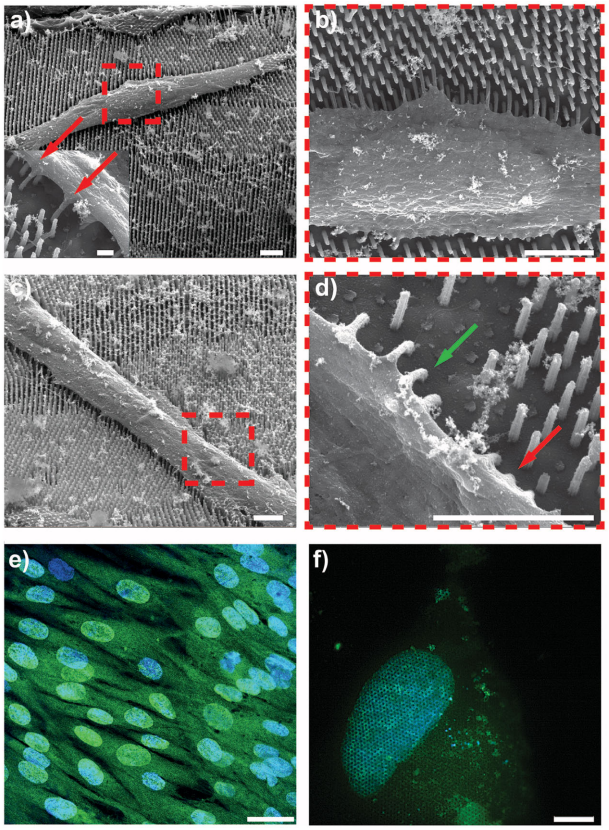

Figure 4. Interaction between primary hDPSC and VA-SiNW arrays. a) SEM image of hDPSC adhering to an array of SiNW of 0.6 NW µm^{-2} in density (with average diameter of 330 nm and NW average heights of 1.2 µm), showing close cell–SiNW contacts. The NW can be observed as protrusions on the top side of the cells edges. Inset: SiNW elements are tightly wrapped within the cell membrane, red arrows. b) Zoomed-in image of (a) showing cell membrane conformation to SiNW elements, with inward deflecting NW tips at the cell periphery. c) Elongated hDPSC showing protrusions from the main cell body. d) A zoomed-in image of (c) showing the close interaction between the NW and the hDPSC membrane. NWs are flexible enough to be bent as the cells generate a traction force (green arrow). NW elements are seen largely embedded within the membrane, without apparent membrane rupturing at the site of NW contact (red arrow). All scale bars 5 µm and a) inset 1 µm. Inverted confocal fluorescence image of eGFP transfected hDPSC (green color) cultured on VA-SiNW arrays. SiNW elements of 3.5 µm average height, 1 NW µm^{-2} density, and 330 nm diameter were used. SiNW elements appear as individual black dots under the hDPSC. Scale bar represents 25 µm. f) Super-resolution structured illumination microscopy image of primary hDPSC transfected using VA-SiNW arrays. SiNW elements of 1.2 µm average height, 1 NW µm^{-2} density, and 330 nm diameter were used. Again, SiNW elements appear as individual black dots under the hDPSC. All cells were costained with nuclear dye Hoechst 33342 (blue color). Scale bar represents 10 µm.

The fundamental mechanisms of NW cell penetration are still unclear.[20,57,58] It is also still unknown to what degree the transfection efficiency depends on the amount of SiNW transversing the cell membrane. Here, using FIB-SEM we observed NW penetration through the cell membrane into the cytoplasm for SiNW arrays with heights ranging from 1.2 to 3.5 μm for hDPSC (**Figure 5**a,b) and for HEK 293 cells (Figure 5c–e). We found only a fraction of SiNW transversed the cell membrane, in agreement with other reports that penetration is a rare, stochastic event.[23,59,60] At low NW heights (<0.4 μm), no penetration of the cell membrane was observed (Figure 5f and Figures S8a–c and S9a–d, Supporting Information).

At NW heights above 3.5 μm, cell behavior changed markedly. FIB-SEM revealed a reduction in the likelihood of membrane penetration for all of the four examined cell types, which we attribute to lower cell adhesion. HEK293 (Figure S11a,b, Supporting Information) and hDPSC (Figure 3e and Figure S11e,f, Supporting Information) clearly adhered poorly to longer NW. "Footprint" artefacts remained on SiNW arrays after cells attached to the VA-NW array and subsequently were lifted off the surface (Figures S11e (inset) and S5b (inset), Supporting Information). These imprints were not visible on VA-NW arrays of shorter NW. The same type of behavior was noted for HFF cultured on long NW (Figure S11c,d, Supporting Information). In accordance with those results, lower numbers of cells were observed on the long NW substrates in fluorescence microscopy (Figures S6 and S7, Supporting Information). Increased NW height has been reported to lead to reduced cell adhesion, a decrease in the individual cell area, and decreased number of focal adhesion complexes.[31,39] This may explain the lower number of transfected cells that we observed on the SiNW arrays with 6.3 μm average height. Cell adhesion has been proposed as the dominant mechanism that governs cell impalement by NW.[20]

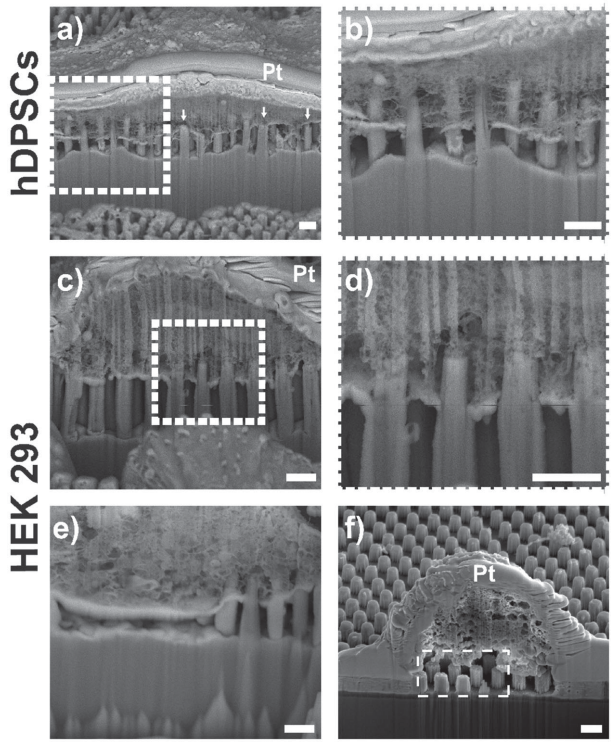

Figure 5. The cell membrane is penetrated by SiNW elements. a) Representative FIB-SEM images showing primary hDPSC penetrated by SiNW. White arrows indicate NWs which did not penetrate the cell membrane. b) Zoom-in of (a) a fraction of SiNW are indeed able to penetrate the cell, despite their relatively large diameter. c) FIB-SEM images showing NW of average 3 μm height were able to penetrate into HEK293. d) zoom-in of (c). e) FIB-SEM images indicating that NW with an average height of 1.2 μm (e) are also capable of breaching the HEK293 membrane, f) while NW with an average height of 0.4 μm are not capable of breaching the HEK293 membrane. White dashed box highlights the fact that the short NWs did not penetrate the cell membrane. All scale bars represent 1 μm.

We also noticed the bending of long SiNW as a result of cell traction forces (Figures S11e (inset) and S5b (inset), Supporting Information). Although the SiNWs are mechanically rigid and maintain vertical alignment before interacting with cells, they are flexible enough to bend.[61] Others reported similar observations of NW bending due to cell traction forces.[61,62] Prompted by these observations, we considered the SiNW stiffness a factor that could play a role in the interaction between the cells and the VA-SiNW arrays. By combining Hooke's law and Euler–Bernoulli Beam theory (Equation (1)), we calculated the theoretical SiNW spring constants, (K_X), as a way of measuring the stiffness of the SiNW.[31] The calculated SiNW spring constant varied inversely to SiNW length (**Table 1**). Longer SiNW are substantially more flexible than shorter NW, and more likely to bend in response to cell traction forces. Bending of NW away from the vertical alignment would be expected to limit the insertion of NW into the cell interior.[20] Cell penetration occurs soon within the first hour of NW contact, furthermore, penetrance is often transient.[21,60] Thus, if NW bend during this critical time window when NWs are able to penetrate the cell membrane and underlying cytoskeleton, transfection efficiency may be compromised.

The FIB-SEM investigation indicates that enhanced interaction between cells and NW elements occurs when the NW height is between 1.2 and 3.5 μm. Direct cell membrane penetration was observed for NW average heights of 1.2–3.5 μm. In contrast, very short (<0.4 μm) and long NW (>3.5 μm), hardly penetrated the cell body. Our observations suggest that most NW remain outside the cell body; even at optimal geometries only a small subset of NW penetrates the cell membrane. Close interaction of cell membranes with NW elements was common to all geometries. We suggest that higher transfection efficiency does not depend solely on penetration; alternatively, upregulation of endocytic trafficking of DNA, driven by local membrane deformation together with increased contact with NW DNA-coated surfaces, could also enhance transfection efficiency.[59,63,64]

2.6. Differences in Transfection Efficiency across Cell Types

Whilst hDPSC and HEK293 cell transfection approached 90% when optimal NW geometries were applied, HFF and HeLa transfection efficiency remained below 65% throughout the study. HeLa cells stood out amongst the four cell types tested for their overall poor transfection efficiency regardless of the NW geometry tested. Low transfection efficiency of HeLa has

Table 1. The spring constant of NW elements within VA-NW arrays varies inversely with NW height.

Average diameter [nm]	400	400	400	400
Average length [μm]	0.4	1.2	3.5	6.3
Spring constant K_x [μN m^{-1}]	1.7×10^{10}	1.0×10^{9}	2.5×10^{7}	4.4×10^{6}

been observed previously. We noticed that HeLa cells had a tendency to proliferate as colonies (Figure S12, Supporting Information) that may prevent efficient NW penetration. Cell division of the more easily transfected HEK 293 on NW structures, by contrast, is characterized by the repeated impaling of daughter cells after each division.[30]

HeLa cells were less adherent to the SiNW surfaces than HEK293 or DPSC, as exemplified by their rounded morphology (Figure S9 and Figures S10c,d and S12, Supporting Information). This is consistent with a report by Kim et al. where HeLa cells displayed weak adhesion on VA-SiNW arrays due to a reduced number of focal adhesion complexes.[39]

HFF cells also exhibited sparser cell attachment and lower cell area on the VA-NW arrays (Figures S6, S7, and S10e,f, Supporting Information), possibly indicating similarly compromised cell adhesion to NW. Overall, we observed that cell types with increased interaction with the VA-NW substrate, i.e., highly adhesive, broadly spread cells, were more efficiently transfected with VA-NW arrays. This may be a consequence of each well-adherent cell simply interacting with a greater number of NW overall, thereby increasing the probability of penetration occurring.

3. Conclusions

We have examined the role of geometric parameters of VA-SiNW arrays in controlling cell behavior and transfection efficiency, using SiNW fabricated via NSL and tMACE techniques. NSL/tMACE is a low-cost and easy-to-implement fabrication method of SiNW arrays; our method brings the technology of SiNW-mediated transfection into the reach of laboratories without access to specialized fabrication facilities. Through the control over SiNW parameters, enabled by NSL in combination with tMACE, we have observed that the transfection efficiency strongly depends on NW height and varies greatly between cell types. For the majority of the tested cell types, medium heights (1.2–3.5 μm), small diameters (<400 nm), and densities between 0.6 and 1.0 NW μm^{-2} were associated to high transfection efficiency. We have observed direct evidence that cells exhibiting high transfection efficiency were impaled by SiNW arrays without the application of any external force. Given the significant amount of progress in this rapidly expanding field, we are confident that this work will be instrumental in designing novel effective SiNW-based transfection platforms.

4. Experimental Section

Chemicals and Materials: All chemicals were obtained from commercial sources and used without further purification. Sulfuric acid (H_2SO_4, 95%–97%) and hydrofluoric acid (HF, 48%) were purchased from Scharlau Chemie (Chem-Supply Pty. Ltd. Australian representation). Hydrogen peroxide (H_2O_2, 30%) was from Merck (Australia). Nitric acid (HNO_3, 70%), hexane (≥95%), 2-propanol (≥99.8%), poly-D-lysine hydrobromide for cell culture (P7280), propidium iodide, and fetal bovine serum were all obtained from Sigma-Aldrich (Australia). P-type silicon wafers, 3–6 Ω cm, ⟨100⟩ were purchased from Siltronix (France). Polybead microspheres solutions (1 μm (07310), and 0.5 μm (0869), 2.5% w/v) were purchased from Polysciences, Inc. (USA) and amidine PSNS (0.5 μm, (A37317), 4% w/v) were obtained from Life Techologies, USA). The gWiz high-expression enhanced green fluorescent protein vector (gWiz eGFP) was purchased from Aldevron (USA). The Click-iT proliferation assay kit, fluorescein diacetate, 100× L-glutamine-penicillin-streptomycin supplement Opti-MEM medium and Hoechst 33342 fluorescent stains were obtained from Life Technologies.

Preparation of Si Wafers: Prior to the PSNS deposition, flat silicon wafers (p-type, 3–6 Ω cm, ⟨100⟩) were cut into roughly 1 × 1 cm^2 pieces and cleaned by sonication in 1:1 solution of ethanol:acetone for 5 min, then sonicated again in MilliQ water (R = 18.2 Ω) for 5 min. This was followed by dipping the wafers into boiling Piranha solution (2:1 H_2SO_4:H_2O_2 v/v, 75 °C) for 1 h to remove organic contaminants, then washing with MilliQ water and drying under a N_2 jet. Prior to PSNS monolayer assembly, samples were treated with O_2 plasma in an RF power system at 50 W and at an O_2 flow rate of 15 cm^3 min^{-1}.

Assembly of Ordered, Uniform PSNS Arrays: Spin Coating: We used a commercial colloidal suspension of PSNS with mean diameters of 0.5 and 1 μm. An aliquot of 50 μL was deposited on clean wafers, then spin-coated (Laurell Technologies, WS-650MZ-23NPP spin-coater, USA) at 200 rpm to form a self-assembled, hexagonally arranged monolayer of PSNS on the wafer surface. This was immediately followed by a 20 s duration spin cycle at 1500 rpm to remove any excessive solution present around the edges of the wafer. A close-packed PSNS monolayer was hence deposited on the silicon surface.

Convective Assembly Deposition: Hexagonal close-packed PSNS monolayers were also deposited over ≈5 cm^2 by convective assembly. The apparatus included a mounted microscope slide that was used as a blade for the PSNS depositions, 50 mm motorized translation stage (MTS50-Z8), a digital camera, and a TMC 66 series csp vibration isolation system. The blade was adjusted to leave a small space between the bottom edge of the blade and the Si substrate. Then ≈50 μL of a suspension of PSNS (either 1 μm or 500 nm in diameter) was injected into the space between the blade and the sample using a microneedle, forming a meniscus between the pinned substrate and the bottom edge of the blade. This resulted in a continuous contact line of PSNS suspension on the Si substrate. To deposit PSNS in a uniform monolayer, operating parameters such stage velocity and PS suspension concentration were adjusted. To monitor the uniformity of the assembly, the process was observed with a digital camera throughout.

Liquid–Liquid Interface (SALI) Deposition: A 50 mL polypropylene centrifuge tube was filled with 40 mL Milli-Q water. The wafer was lowered into the water on a holder with an angle of 30°, and 7 mL of hexane (≥95%) was added carefully on top. A needle connected to a peristaltic pump containing 0.02%–0.08% solution of amidine PSNS (500 nm diameter) in a 60:40 mixture of Milli-Q water:2-propanol was inserted into the centrifuge tube and the tip of the needle positioned at the interface between the hexane and water. The solution was then injected at a speed of 0.5 μL s^{-1} to a specified volume and the needle withdrawn. The PSNS at the interface rearranged into open crystals, due to the long-range electrostatic repulsions between them. Next, the wafer was extracted at 25 μm s^{-1} through the water–hexane interface and subsequently the hexane–air interface. To ensure transfer of the interfacial crystalline pattern, the speed of extraction was controlled to be equal to (or lower than) the rate of hexane evaporation to prevent a drying meniscus forming across the sample, which can lead to PSNS rearrangement.

Preparation of VA-SiNW Arrays: Samples prepared by spin coating and convective assembly strategies were inserted into the O_2 plasma etcher and Ag sputter coater using an HHV TF600 sputter coater. The O_2 plasma

was generated with an radio frequency (RF) power system at 50 W and at an O_2 flow rate of 15 cm^3 min^{-1}. All plasma etching treatments were conducted for duration at a pressure of 2.00×10^{-2} mbar. 1 μm PSNS were etched at different plasma etching time (25, 40, and 50 min), in order to achieve three types of diameters (330, 400, and 600 nm). 0.5 μm PSNS were etched for 15 min, in order to achieve a diameter of 330 nm. Ag sputter coating was carried out using a DC power supply set at 100 W with a flow rate of Ar gas set at 10 cm^3 min^{-1} to generate a pressure of 1.00×10^{-2} mbar inside the chamber. All sputter coating was performed for a total of 3–4 min to generate a 20–40 nm layer of Ag. The PSNS were then removed by sonication in MilliQ water for 1 min. tMACE was carried out in a 15 mL standard Teflon container by diluting HF (48%) and H_2O_2 in MilliQ water. All etching solutions were prepared with HF concentrations of 4.8 and 0.13 M H_2O_2. The Teflon container was sealed and the reactions were conducted only at room temperature for different time durations (2, 10, 40, and 70 min) to achieve the desired SiNW length. These etching times can vary slightly according to the NW diameter that is being fabricated.

SiNW Stiffness Calculation: Equation (1), K_x is the spring constant of the SiNW, d is the SiNW diameter, L is the SiNW length, and E is the Young's modulus for Si (100) ($E = 170$GPa).

$$K_X = \frac{d^4 E}{4L^3} \quad (1)$$

SiNW Degradation Assay: Silicic acid produced during SiNW degradation was determined by means of an ammonium molybdate colorimetric assay. Pieces of 1 cm^2 preweighed substrates of SiNW arrays were immersed into separate 20 mL solutions of 0.25 M tris(hydroxymethyl)aminomethane hydrochloride (Tris–HCl) (pH 7.2). Tris buffer was used instead of phosphate buffered saline (PBS) since phosphate in the PBS intereferes with the assay. As a control sample, a flat piece of Si wafer was also subjected to the same treatment. The SiNW array substrates were tested over a total period of 10 d. Each day, 40 μL of the silicic acid-containing solution was removed and acidified with 40 μL of 0.3 M HCl solution. This was followed by adding 20 μL of a 42×10^{-3} M ammonium molybdate ($(NH_4)_2MoO_4$) solution and incubating the mixture for 10 min. Next, 20 μL of the chelating agent ethylenediaminetetraacetic acid (EDTA, 27×10^{-3} M) and 40 μL of 1.35 M sodium sulfite (Na_2SO_3) were added. After incubation at room temperature for 1 h, spectrophotometric analysis (microplate reader, VMax, Molecular Devices, USA) at 640 nm was performed. Silicic acid concentration standards were prepared with sodium metasilicate pentahydrate ($Na_2SiO_3 \times 5H_2O$) and were used for calibration curve covering the range of $(0–100) \times 10^{-6}$ M. The data were adjusted to show the percentage mass loss per gram of sample.

Cell Culture: Four types of human cells were investigated: human dental pulp mesenchymal stem cells (hDPSC), HFF, human embryonic kidney cells (HEK293, ATCC CRL-1573) cells, and HeLa cells (ATCC CCL-2). All cells were grown and maintained at 37 °C with 5% CO_2 in Dulbecco's modified Eagle's medium (DMEM) supplemented with 10% fetal bovine serum (FBS), 2×10^{-3} M L-glutamine, 100 U mL^{-1} penicillin, and 100 g mL^{-1} streptomycin, for 2–3 d until they were 70%–80% confluent. After trypsinization, cells were seeded at a density of 1×10^5 cells mL^{-1} in complete DMEM onto the substrates.

Cell Viability Assay: The viability of cells on VA-NW arrays was assayed by live–dead staining using a final concentration of 15 μg mL^{-1} FDA and 5×10^{-3} M PI in PBS for 3 min at 37 °C. After staining, samples were rinsed with PBS before being observed under an inverted Nikon Ti-S fluorescence microscope (Nikon, Japan) using standard filters for FITC (fluorescein isocyanate, 495 nm excitation/517 nm emission) for FDA and TRITC (tetramethylrhodamine, 538 nm excitation/619 nm emission nm) for PI. Observations were conducted at three different locations on the surface of each sample at magnification of the 20x objective lens. All experiments were repeated at least three times.

Cell Proliferation Assay: To measure cell proliferation, the Click-iT EdU Assay was used. EDU is a nucleoside analog of thymidine and is incorporated into the DNA of replicating cells, to distinguish proliferating from resting cells. Briefly, cells were seeded at density of 5×10^4 cells mL^{-1} onto surfaces and incubated at 37 °C and 5% CO_2 for 48 h. For labeling cells with EdU, equal volume of 20×10^{-6} M EDU solutions was added to the cells and incubated at 37 °C and 5% CO_2 for 60 min, followed by the removal of the medium. The cells were then fixed for 20 min in a solution containing 4% paraformaldehyde at room temperature and washed with 1 mL 3% BSA in PBS and subsequently permeablized with 0.2% Triton X-100 in PBS for 5 min at room temperature. In this assay, detection of the signal is based on a click reaction between the EDU and the Alexa Fluor 647 dye. The Click-iT EDU reaction cocktail was prepared according to the manufacturer's instructions, added to the cells and incubated for 30 min in the dark at room temperature. Following removal of Click-iT reaction cocktail, the cells were washed twice in 1 mL 3% bovine serum albumin (BSA) in PBS. To count total cell numbers, nuclei were counter stained by using a final concentration of 2 μg mL^{-1} Hoechst 33342. The percentage of proliferation of cells on flat silicon as a control and SiNW arrays was determined by counting EDU-positive cells (red fluorescence) versus total number of cells, indicated by nuclear Hoechst 33342 staining (blue fluorescence).

Cell Transfection: Cells were cultured in DMEM medium supplemented with 10% FBS, 2×10^{-3} M L-glutamine, 100 U mL^{-1} penicillin, and 100 g mL^{-1} streptomycin, then incubated at 37 °C in a fully humidified atmosphere with 5% CO_2, medium was exchanged twice a week. The adherent cells were detached and harvested by using 0.05% trypsin/EDTA solution treatment. Serial passaging (1:3 split) at 70%–80% confluence was performed.

To transfect gWIZ GFP plasmid into human cells, we placed the VA-NW substrates in a 24-well sterile format. The substrates were then sterilized in 70% ethanol and were allowed to dry at room temperature for 2 h in a laminar flow cabinet. Following this, the substrates were coated with poly-D-lysine at concentration of 167 μg L^{-1} and incubated at 4 °C for 4 h, followed by washing step with PBS. gWIZ GFP plasmid was diluted to 20 μg mL^{-1} in PBS and 100 μL of this solution was add per well on top of the substrate. The substrates were then incubated at 4 °C overnight and unbound plasmid was washed with PBS. Cells were seeded at density of 1×10^5 cells mL^{-1} in Opti-MEM onto the substrates. The samples were then incubated for 4–6 h at 37 °C in a humidified atmosphere with 5% CO_2. Subsequently, the Opti-MEM medium was replaced with regular medium containing DMEM, FBS 10% and incubated overnight at 37 °C for 48–72 h.

Determination of Transfection Efficiency: To assess the efficiency of delivery of eGFP reporter gene, the fraction of cells containing that plasmid was determined after 60 h of incubation. For each combination of NW height, diameter, and density examined, $N \geq 3$ independent arrays were fabricated and transfection assessed on three fields of view chosen at random on each array. Images were independently scored for transfection efficiency using the WimTransfection algorithm (Wimasis, Munich, Germany). Transfection efficiency is reported as average ± standard deviation in Figures 2 and 3 (Tables S1–S4, Supporting Information) to indicate the reproducibility of transfection on independently fabricated NW arrays. Statistical analysis of transfection efficiency data was carried out on data pooled for each parameter combination using Fisher's exact test,[65,66] applying Bonferroni correction for multiple comparisons.[67]

Surface Characterization—AFM Imaging: Surface roughness measurements were taken from AFM images generated using a JPK NanoWizard III (JPK Instruments, Berlin). Imaging was performed in AC mode (aka Tapping Mode) using AppNano probes (ACT Series, Applied NanoStructures, Inc, CA). Each image was recorded at 1 Hz. Resolutions were 1500×1250 and 1500×199 for the SiNW and zoomed-in section (a), respectively.

Surface Characterization—FIB-SEM Imaging: The Helios Nanolab 600 dual beam FIB-SEM (FEI, North America NanoPort) was used to investigate the interaction between the SiNW arrays and the cells. The NW arrays were coated with poly-D-lysine solution before cell plating. All of the examined four cells were seeded at a density of 1×10^5 cells mL^{-1} in complete DMEM onto the substrates at 37 °C and 5% CO_2. For cell

SEM samples, specimens were prepared by means of a critical point drying process before imaging. Cell samples were fixated with 4% paraformaldehyde solution for 30 min at room temperature, followed by washing in PBS buffer at pH 7.4. The cells underwent postfixation with 1% osmium tetroxide. After rinsing with PBS buffer, the cell specimens were gradually dehydrated with increasing concentrations of ethanol for 15 min (50%, 70%, 90%, and 100%), and finally critical point dried (Tousimis931). Some of the samples were chemically dried with hexamethyldisilazane (HMDS). For this purpose, cell specimens were gradually dehydrated with (3:1, 1:1, 1:3 EtOH:HMDS), and then 100% HMDS and allowed to dry in air. Finally, all substrates were mounted on SEM stubs. This was followed by 10 nm carbon coating with the help of a sputter coater to increase the conductivity of the specimen. In FIB-SEM, 1–2 µm thick platinum was deposited at 30 kV with 0.46 nA current in the region of interest to protect it from ion-beam-induced damage. Rough milling followed by polishing was carried out with decreasing current from 2.8 nA to 93 pA in several steps at 30 kV. Final polishing was carried out at 30 kV with 28 pA current.

Surface Characterization—SEM Imaging: SEM imaging was carried out using a Quanta 450 FEG Environmental SEM (FEI, Netherlands) fitted with a solid-state detector and operating at 5–30 kV in high vacuum mode.

Surface Characterization—TEM Imaging: TEM analysis was performed on a JEOL JEM-2100F field-emission gun TEM after removal of the SiNW by sonication from the array substrate. The SiNW were then suspended in isopropanol to ensure the rapid evaporation of the solvent when deposited on a 75 (lines $inch^{-1}$) copper grid (SPI # 2007C-XA, SPI Supplies).

Surface Characterization—Confocal and SR-SIM Imaging: The cell samples were washed with PBS and then fixed in a solution of 4% paraformaldehyde in PBS (PH = 7.4) for 10 min, followed by permeabilization in PBS-0.25% Triton X-100 for 5 min at room temperature. After washing three times for 5 min each at room temperature in PBS, the nuclei were stained with Hoechst 33342 at a final concentration of 5 µg mL^{-1} for 15 min at room temperature. Confocal imaging was carried out using a Nikon A1R confocal laser scanning microscope system. eGFP and Hoechst 33342 fluorescence were excited using the 488 nm argon laser line and the 405 nm laser, respectively. The fixed hDPSC were analyzed determined using the Nikon NIS-Elements software provided by the manufacturer. SR-SIM imaging was carried out using a Zeiss 780 in the ELYRA mode. The fixed hDPSC were analyzed determined using the Zeiss 780 ZEN 2012 software provided by the manufacturer.

Image Processing and Analysis: Fluorescence microscopy images were statistically analyzed by Wimasis Image Analysis. SEM Images were processed and analyzed with Image J. The contrast and the brightness were not varied from the original SEM pictures. For data analysis and plotting, we used Origin 8.2 (OriginLab).

Supporting Information

Supporting Information is available from the Wiley Online Library or from the author.

Acknowledgements

R.E., B.D., and D.B. contributed equally to this work. This research was conducted and funded by the Australian Research Council Centre of Excellence in Convergent Bio-Nano Science and Technology (Project No. CE140100036). Funding from the German Academic Exchange Service–Australian Technology Network of Universities (DAAD-ATN) Joint Research Co-operation Scheme is also kindly acknowledged. This work was in part performed at the South Australian node of the Australian National Fabrication Facility (ANFF) under the National Collaborative Research Infrastructure Strategy to provide nano- and microfabrication facilities for Australia's researchers. The authors would like to thank Marc Cirera for providing us with the schematic representation of the fabrication process shown in Scheme 1 and for the TOC. N.H.V. was supported by an Alexander von Humboldt Foundation Fellowship. L.I. acknowledges financial support from the Swiss National Science Foundation grant PP00P2_144646/1 and Nicholas D. Spencer for infrastructural support. Funding from the German Science Foundation (DFG), in the framework of Priority Programme 1420, is also acknowledged.

Received: August 17, 2015
Published online: October 13, 2015

[1] A. Pfeifer, I. M. Verma, *Annu. Rev. Genomics Hum. Genet.* **2001**, *2*, 177.
[2] A. C. Nathwani, E. G. Tuddenham, S. Rangarajan, C. Rosales, J. McIntosh, D. C. Linch, P. Chowdary, A. Riddell, A. J. Pie, C. Harrington, J. O'Beirne, K. Smith, J. Pasi, B. Glader, P. Rustagi, C. Y. Ng, M. A. Kay, J. Zhou, Y. Spence, C. L. Morton, J. Allay, J. Coleman, S. Sleep, J. M. Cunningham, D. Srivastava, E. Basner-Tschakarjan, F. Mingozzi, K. A. High, J. T. Gray, U. M. Reiss, A. W. Nienhuis, A. M. Davidoff, *N. Engl. J. Med.* **2011**, *365*, 2357.
[3] R. E. MacLaren, M. Groppe, A. R. Barnard, C. L. Cottriall, T. Tolmachova, L. Seymour, K. R. Clark, M. J. During, F. P. Cremers, G. C. Black, A. J. Lotery, S. M. Downes, A. R. Webster, M. C. Seabra, *Lancet* **2014**, *383*, 1129.
[4] R. Brentjens, R. Yeh, Y. Bernal, I. Riviere, M. Sadelain, *Mol. Ther.* **2010**, *18*, 666.
[5] D. Lechardeur, A. S. Verkman, G. L. Lukacs, *Adv. Drug Delivery Rev.* **2005**, *57*, 755.
[6] A. K. Shalek, J. T. Robinson, E. S. Karp, J. S. Lee, D. R. Ahn, M. H. Yoon, A. Sutton, M. Jorgolli, R. S. Gertner, T. S. Gujral, G. MacBeath, E. G. Yang, H. Park, *Proc. Natl. Acad. Sci. USA* **2010**, *107*, 1870.
[7] J. J. VanDersarl, A. M. Xu, N. A. Melosh, *Nano Lett.* **2012**, *12*, 3881.
[8] E. Peer, A. Artzy-Schnirman, L. Gepstein, U. Sivan, *ACS Nano* **2012**, *6*, 4940.
[9] X. Chen, A. Kis, A. Zettl, C. R. Bertozzi, *Proc. Natl. Acad. Sci. USA* **2007**, *104*, 8218.
[10] D. B. Peckys, A. V. Melechko, M. L. Simpson, T. E. McKnight, *Nanotechnology* **2009**, *20*, 145304.
[11] R. Elnathan, M. Kwiat, F. Patolsky, N. H. Voelcker, *Nano Today* **2014**, *9*, 172.
[12] B. Sara, B.-M. Nina, R. R. Katrine, A. Tor Kristian, B. Trine, L. M. Karen, *Nanotechnology* **2014**, *25*, 362001.
[13] W. Kim, J. K. Ng, M. E. Kunitake, B. R. Conklin, P. Yang, *J. Am. Chem. Soc.* **2007**, *129*, 7228.
[14] H. Persson, C. Kobler, K. Molhave, L. Samuelson, J. O. Tegenfeldt, S. Oredsson, C. N. Prinz, *Small* **2013**, *9*, 4006.
[15] P. M. Mendes, *Chem. Soc. Rev.* **2013**, *42*, 9207.
[16] T. Berthing, C. B. Sorensen, J. Nygard, K. L. Martinez, *J. Nanoneurosci.* **2009**, *1*, 3.
[17] S. Qi, C. Yi, S. Ji, C. C. Fong, M. Yang, *ACS. Appl. Mater. Interfaces* **2009**, *1*, 30.
[18] M. S. Chan, P. K. Lo, *Small* **2014**, *10*, 1255.
[19] I. Y. Wong, S. N. Bhatia, M. Toner, *Genes Dev.* **2013**, *27*, 2397.
[20] X. Xie, A. M. Xu, M. R. Angle, N. Tayebi, P. Verma, N. A. Melosh, *Nano Lett.* **2013**, *13*, 6002.
[21] A. M. Xu, A. Aalipour, S. Leal-Ortiz, A. H. Mekhdjian, X. Xie, A. R. Dunn, C. C. Garner, N. A. Melosh, *Nat. Commun.* **2014**, *5*, 3613.
[22] T. E. McKnight, A. V. Melechko, D. K. Hensley, D. G. J. Mann, G. D. Griffin, M. L. Simpson, *Nano Lett.* **2004**, *4*, 1213.

[23] T. Berthing, S. Bonde, K. R. Rostgaard, M. H. Madsen, C. B. Sorensen, J. Nygard, K. L. Martinez, *Nanotechnology* **2012**, *23*, 415102.
[24] X. Xie, A. M. Xu, S. Leal-Ortiz, Y. Cao, C. C. Garner, N. A. Melosh, *ACS Nano* **2013**, *7*, 4351.
[25] S. W. Han, C. Nakamura, I. Obataya, N. Nakamura, J. Miyake, *Biosens. Bioelectron.* **2005**, *20*, 2120.
[26] S. W. Han, C. Nakamura, N. Kotobuki, I. Obataya, H. Ohgushi, T. Nagamune, J. Miyake, *Nanomedicine* **2008**, *4*, 215.
[27] A. K. Shalek, J. T. Gaublomme, L. Wang, N. Yosef, N. Chevrier, M. S. Andersen, J. T. Robinson, N. Pochet, D. Neuberg, R. S. Gertner, I. Amit, J. R. Brown, N. Hacohen, A. Regev, C. J. Wu, H. Park, *Nano Lett.* **2012**, *12*, 6498.
[28] C. Chiappini, J. O. Martinez, E. De Rosa, C. S. Almeida, E. Tasciotti, M. M. Stevens, *ACS Nano* **2015**, *9*, 5500.
[29] C. Chiappini, E. De Rosa, J. O. Martinez, X. Liu, J. Steele, M. M. Stevens, E. Tasciotti, *Nat. Mater.* **2015**, *14*, 532.
[30] S. Bonde, T. Berthing, M. H. Madsen, T. K. Andersen, N. Buch-Manson, L. Guo, X. Li, F. Badique, K. Anselme, J. Nygard, K. L. Martinez, *ACS Appl. Mater. Interfaces* **2013**, *5*, 10510.
[31] S. W. Kuo, H. I. Lin, J. H. Ho, Y. R. Shih, H. F. Chen, T. J. Yen, O. K. Lee, *Biomaterials* **2012**, *33*, 5013.
[32] C. Y. Yang, L. Y. Huang, T. L. Shen, J. A. Yeh, *Eur. Cells Mater.* **2010**, *20*, 415.
[33] S. Qi, C. Yi, W. Chen, C. C. Fong, S. T. Lee, M. Yang, *ChemBioChem* **2007**, *8*, 1115.
[34] G. Piret, M.-T. Perez, C. N. Prinz, *RSC Adv.* **2014**, *4*, 27888.
[35] A. M. Morales, C. M. Lieber, *Science* **1998**, *279*, 208.
[36] Z. P. Huang, H. Fang, J. Zhu, *Adv. Mater.* **2007**, *19*, 744.
[37] Z. Huang, N. Geyer, P. Werner, J. de Boor, U. Gosele, *Adv. Mater.* **2011**, *23*, 285.
[38] L. Isa, K. Kumar, M. Muller, J. Grolig, M. Textor, E. Reimhult, *ACS Nano* **2010**, *4*, 5665.
[39] S. Y. Kim, E. G. Yang, *Nanotechnology* **2013**, *24*, 455704.
[40] G. Piret, E. Galopin, Y. Coffinier, R. Boukherroub, D. Legrand, C. Slomianny, *Soft Matter* **2011**, *7*, 8642.
[41] D. J. Kim, G. Lee, G. S. Kim, S. K. Lee, *Nanoscale Res. Lett.* **2012**, *7*, 637.
[42] Q. Ha, G. Yang, Z. Ao, D. Han, F. Niu, S. Wang, *Nanoscale* **2014**, *6*, 8318.
[43] J. J. Hill, K. Haller, B. Gelfand, K. J. Ziegler, *ACS Appl. Mater. Interfaces* **2010**, *2*, 1992.
[44] C. Chiappini, X. Liu, J. R. Fakhoury, M. Ferrari, *Adv. Funct. Mater.* **2010**, *20*, 2231.
[45] J. L. Coffer, *Semiconducting Silicon Nanowires for Biomedical Applications*, Woodhead Publishing Ltd, Cambridge, UK **2014**.
[46] S. P. Khan, G. G. Auner, G. M. Newaz, *Nanomedicine* **2005**, *1*, 125.
[47] L. E. Bain, A. Ivanisevic, *Small* **2015**, *11*, 768.
[48] C. Xie, L. Hanson, W. Xie, Z. Lin, B. Cui, Y. Cui, *Nano Lett.* **2010**, *10*, 4020.
[49] X. Wei, X. Yang, Z. Han, F. Qu, L. Shao, Y. Shi, *Acta Pharmacol. Sin.* **2013**, *34*, 747.
[50] L. Yan, J. Zhang, C. S. Lee, X. Chen, *Small* **2014**, *10*, 4487.
[51] X. Chen, G. Zhu, Y. Yang, B. Wang, L. Yan, K. Y. Zhang, K. K. Lo, W. Zhang, *Adv. Healthcare Mater.* **2013**, *2*, 1103.
[52] M. R. Angle, A. Wang, A. Thomas, A. T. Schaefer, N. A. Melosh, *Biophys. J.* **2014**, *107*, 2091.
[53] A. S. Togonal, L. He, P. Roca i Cabarrocas, Rusli, *Langmuir* **2014**, *30*, 10290.
[54] N. Buch-Månson, S. Bonde, J. Bolinsson, T. Berthing, J. Nygård, K. L. Martinez, *Adv. Funct. Mater.* **2015**, *25*, 3246.
[55] Z. Jahed, S. Molladavoodi, B. B. Seo, M. Gorbet, T. Y. Tsui, M. R. Mofrad, *Biomaterials* **2014**, *35*, 9363.
[56] T. D. Nguyen-Vu, H. Chen, A. M. Cassell, R. J. Andrews, M. Meyyappan, J. Li, *IEEE Trans. Biomed. Eng.* **2007**, *54*, 1121.
[57] L. Hanson, Z. C. Lin, C. Xie, Y. Cui, B. Cui, *Nano Lett.* **2012**, *12*, 5815.
[58] W. Hallstrom, T. Martensson, C. Prinz, P. Gustavsson, L. Montelius, L. Samuelson, M. Kanje, *Nano Lett.* **2007**, *7*, 2960.
[59] F. Mumm, K. M. Beckwith, S. Bonde, K. L. Martinez, P. Sikorski, *Small* **2013**, *9*, 263.
[60] A. Aalipour, A. M. Xu, S. Leal-Ortiz, C. C. Garner, N. A. Melosh, *Langmuir* **2014**, *30*, 12362.
[61] Z. Li, J. Song, G. Mantini, M. Y. Lu, H. Fang, C. Falconi, L. J. Chen, Z. L. Wang, *Nano Lett.* **2009**, *9*, 3575.
[62] R. Wierzbicki, C. Købler, M. R. B. Jensen, J. Łopacińska, M. S. Schmidt, M. Skolimowski, F. Abeille, K. Qvortrup, K. Mølhave, *PLoS One* **2013**, *8*, e53307.
[63] A. F. Adler, K. W. Leong, *Nano Today* **2010**, *5*, 553.
[64] J. Liu, Y. Sun, G. F. Oster, D. G. Drubin, *Curr. Opin. Cell Biol.* **2010**, *22*, 36.
[65] J. H. McDonald, *Handbook of Biological Statistics*, 3rd ed., Sparky House Publishing, Baltimore, MD **2014**.
[66] A. Agresti, *Stat. Sci.* **1992**, *7*, 131.
[67] P. L. MacDonald, R. C. Gardner, *Educ. Psychol. Meas.* **2000**, *60*, 73.